Fault Detection and Isolation Filters for Three-Phase AC-DC Power Electronics Systems

Xiangyu Ding, *Student Member*, IEEE, Jason Poon, *Student Member*, IEEE,
Ivan Čelanović, *Member*, IEEE, and Alejandro D. Domínguez-García, *Member*, IEEE

***Abstract*—This paper develops and experimentally demonstrates a new class of high-fidelity model-based fault detection and isolation filters for three-phase AC-DC power electronics systems. The structure of these filters is similar to that of a piecewise linear observer and in the absence of faults the filter residual converges to zero. On the other hand, whenever a fault occurs, by appropriately choosing the filter gain, the filter residual will exhibit certain geometric characteristics that allow the fault to be detected and, in certain cases, also isolated. Key advantages of these filters include fast detection of all possible component faults and the ability to capture slow degradation in individual components. In order to experimentally demonstrate their feasibility, the filters are implemented on an ultra-fast application-specific real-time processor. While the theoretical framework developed is general, the analysis, simulations, and experiments are focused on widely used power electronics systems implementing three-phase AC-DC converters that are used in, e.g., motor drive applications and distributed static compensators.**

***Index Terms*—Fault detection and isolation, observers, three-phase AC-DC converters, field programmable gate arrays.**

I. Introduction

The reliability of power electronics systems is critically important in many applications; ranging from safety- and mission-critical systems in aerospace, automotive, ship and train propulsion; to information technology and communication systems, industrial automation, and converters for voltage and power flow control in electrical networks. In general, in any engineered system, ensuring a high-level of reliability is usually achieved by incorporating mechanisms for fault tolerance into the system design. Fault tolerance is the ability of a system to adapt and compensate, in a systematic way, to random component faults, while providing completely or partially its intended functionality [1]. There are three key elements to any fault-tolerant system design: i) component redundancy, ii) a fault detection and isolation system, and iii) a reconfiguration system that, once a fault has been detected and isolated, substitutes the faulty component by a redundant one, or reconfigures the control to compensate for the fault. In this paper, we propose a new approach to fault detection and isolation (FDI) in power electronics applications, with special emphasis on the class of systems that implement two-level three-phase converters, e.g., inverters for variable-speed drive applications, active filters, and Distributed Static Compensators (D-STATCOMs).

An FDI system (see, e.g., [2]) executes two tasks: i) detection, which makes a binary decision whether or not a fault has occurred, and ii) isolation, which determines the location of the faulty component. Methods for FDI in power electronics applications can be broadly classified into three different classes: i) model-based, uses knowledge of the system model (including the effect of faults) to design residual generators that can point to specific faults (see, e.g., [3], [4], [5], [6], [7]); ii) artificial intelligence-based, uses neural networks and fuzzy logic to develop expert systems that once trained can point to specific faults (see, e.g., [8], [9], [10]); and iii) signal processing-based, uses spectral analysis to identify unique fault signatures (see, e.g., [11], [12]). In this paper, we focus on the model-based class and propose a new FDI method for power electronics systems. Specifically, we extend and generalize the ideas for FDI in linear time-invariant (LTI) systems in [13], [14], to linear-switched systems, which describe, with high-fidelity, the large-signal behavior of a wide range of power electronics systems (see, e.g., [15], [16]).

In the LTI setting, the authors of [13], [14] propose a detection filter with the same structure of a classical Luenberger observer (see, e.g., [17]). In the absence of faults, the filter works in the same way as a Luenberger observer, i.e., the filter asymptotically estimates the actual system states, and therefore the filter residual, which is defined as the difference between the actual system output and the filter output, asymptotically converges to zero. Whenever a fault in a component occurs, the filter residual no longer converges to zero. In general, the fault causes a change in the transition and/or the system input matrices; therefore, the detection filter, designed for estimating the states of the nominal (pre-fault) system, can no longer estimate the states of the post-fault system. Then, the key is to appropriately choose the filter gain so the residual exhibits certain geometric characteristics that allows the fault to be both detected and isolated (i.e., the faulty component can be uniquely identified). As we discuss next, tailoring these ideas (which are well suited for FDI in LTI systems) to power electronics systems is not straightforward.

In power electronics systems, which are fundamentally nonlinear and time-varying, it is common to use small-signal (linearized) average system models to design the controls (see, e.g., [18], [19]). The use of linearized average models together with the observer-based linear filters described above

X. Ding and A. D. Domínguez-García are with the ECE Department of the University of Illinois at Urbana-Champaign, Urbana, IL 61801, USA. E-mail: {ding3,aledan}@ILLINOIS.EDU.

J. Poon and I. Celanovic are with the MIT Institute for Soldier Nanotechnologies, Cambridge, MA 02139, USA. E-mail: {jsn,ivanc}@MIT.EDU.

This work was supported in part by the National Science Foundation (NSF) under Career Award ECCS-CAR-0954420.

appears to be a feasible solution to tackle the FDI problem in power electronics; however, linearized average models cannot properly capture the effect of a fault on the systems dynamics.[1] To overcome the limitations of linearized average models when designing FDI filters for power electronics systems, we propose the use of a large-signal model of the system; specifically a linear-switched state-space model to develop a piecewise linear FDI filter with a similar structure to that of a piecewise linear observer [20].

A piecewise linear FDI filter is comprised of a collection of linear state-space models (subsystems), each of which has the same structure of a Luenberger observer, including the corresponding gain matrix. The transitions between the subsystems are determined by the same rules that govern the switching in the actual system—a challenge is to provide a real-time computational platform that can execute the FDI filter at high-enough speed. Another challenge is to design the individual gain matrices so that i) the detection filter residual exhibits certain geometric characteristics for each particular fault, and ii) the observer is stable. With respect to ii), it is well-known that choosing the individual gains such that each subsystem is stable is not sufficient for ensuring stability (see, e.g., [21]). Thus, as part of the FDI filter design procedure outlined in the paper, we provide sufficient conditions that ensure the choice of gain matrices renders the filter stable.

In order to illustrate the design procedure and the performance of the resulting filters, we provide two simulation-based case studies that involve a three-phase two-level inverter and a D-STATCOM. In addition, we experimentally demonstrate the feasibility of the proposed filters for detecting and isolating faults in a system comprised of a three-phase two-level inverter connected in one end to a voltage source and to a three-phase balanced load in the other. In this regard, in order to realize an FDI filter for such a setting, we need to, essentially, run *in real time*, a copy of the linear-switched state-space model that describes the actual system, including the switching among the subsystems at frequencies that range, depending on the application, from hundreds to thousands of Hz. In order to achieve this, we rely on an application-specific processor architecture tailored for low-latency execution of linear-switched system models [22]. This computational platform enables the simulation of linear-switched state-space models for power electronics converters with a fixed 1 μs time step, including input-output latency, and guarantees the computation time for each time step to be shorter than the 1 μs simulation time step.

The remainder of this paper is organized as follows. Section II introduces the modeling framework adopted throughout the paper. Section III formulates and provides a solution to the FDI filter design problem. Section IV develops and demonstrate an FDI filter for a three-phase inverter connected to a RL load. In Section V, we design an FDI filter for a D-STATCOM. Concluding remarks are presented in Section VI.

[1]This can be easily illustrated in a simple buck converter when there is a fault that causes a change in the capacitance value of the output filter capacitor [4]. While this fault causes an increase in the output voltage ripple that could degrade system performance, this ripple does not manifest in the average model; therefore a linear FDI filter that relies on the average model cannot detect the presence of this fault.

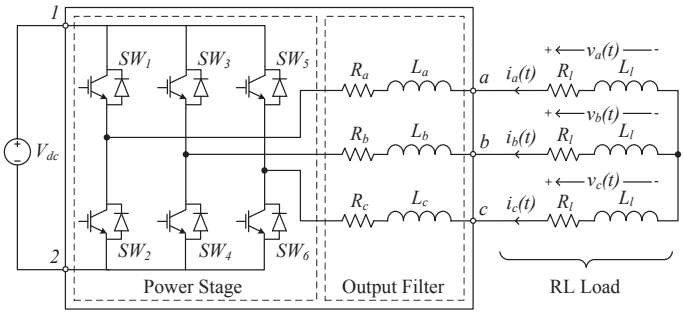

Fig. 1. Inverter with RL load system.

II. Modeling Framework

In this section, we develop the linear-switched system modeling framework adopted throughout the paper and introduce relevant notation and terminology. In order to build the intuition behind the ideas put forward, we start off with the three-phase AC-DC power electronics system in Fig. 1. Then, we generalize the framework to a larger class of three-phase AC-DC power electronics systems.

A. Three-Phase Inverter with RL Load

Consider the three-phase AC-DC power electronics system in Fig. 1, comprised of i) a power stage, and ii) an output filter. The DC voltage source and the RL load, although interconnected to both ends of the system, are not considered part of it, i.e., they are what we refer to as *external elements*. The large-signal dynamics of this AC-DC power electronics system can be accurately represented by *switched system*[2] modeling formalisms. In particular, a switched system can be described by a collection of state-space models—referred to as *subsystems* or *modes*—together with a *switching signal*,[3] the role of which is to specify, at each time instant, the active mode [21]. In the system of Fig. 1, each mode can be obtained by applying Kirchhoff's laws to each of the circuits that results from the possible open/closed switch combinations. The switching signal is defined by the specifics of the control system that determines the switch open/close positions.

TABLE I
Possible open/close switch positions: $s_i = 1$ ($\overline{s}_i = 1 - s_i = 0$) if SW_i is closed and $s_i = 0$ ($\overline{s}_i = 1 - s_i = 1$) if SW_i is open

p	1	2	3	4	5	6	7	8
$s_1/\overline{s}_2$	0	0	0	0	1	1	1	1
$s_3/\overline{s}_4$	0	0	1	1	0	0	1	1
$s_5/\overline{s}_6$	0	1	0	1	0	1	0	1

[2]A dynamical system that can be described by the interaction of some continuous and discrete dynamic behavior is referred to as a *hybrid system*. A *switched system* is a continuous-time system with (isolated) discrete switching events. A switched system can be obtained from a hybrid system by neglecting the details of the discrete behavior [21].

[3]A switching signal is a piecewise constant function with a finite number of discontinuities—the *switching times*—on every bounded time interval, taking a constant value on every interval between two consecutive switching times.

1) Nominal (Pre-Fault) System Model: For the system of Fig. 1, there are six switches, which means that there are 64 possible combinations; however, during normal operation, on each phase, there is exactly one switch closed at any given time, which results in only eight feasible modes. Let $\mathcal{P} = \{1, 2, \ldots, 8\}$ be the set indexing the feasible modes, and let $s_i,\ i = 1, 2, \ldots, 6$, denote an indicator variable that, at time t, takes value 0 whenever switch i (denoted by SW_i) is open, and value 1 whenever it is closed. Then, as defined in Table I, each $p \in \mathcal{P}$ is uniquely defined by an open/closed switch combination $\{s_1,\ s_2, \ldots, s_6\}$; therefore, the active mode at time t can be indicated by a function $\sigma :\ [0, \infty) \to \mathcal{P}$ (the switching signal). Now, by defining $x(t) = [i_a(t), i_b(t), i_c(t)]^T$ and $v(t) = [V_{dc}, v_a(t), v_b(t), v_c(t)]^T$, the system dynamics can be described by a linear-switched state-space model of the form

$$E_{\sigma(t)}\frac{dx(t)}{dt} = F_{\sigma(t)}x(t) + G_{\sigma(t)}v(t), \tag{1}$$

with

$$E_{\sigma(t)} = \begin{bmatrix} L_a & -L_b & 0 \\ 0 & L_b & -L_c \\ 1 & 1 & 1 \end{bmatrix},$$

$$F_{\sigma(t)} = \begin{bmatrix} -R_a & R_b & 0 \\ 0 & -R_b & R_c \\ 0 & 0 & 0 \end{bmatrix},$$

$$G_{\sigma(t)} = \begin{bmatrix} -\frac{(s_1-s_2)-(s_3-s_4)}{2} & 1 & -1 & 0 \\ -\frac{(s_3-s_4)-(s_5-s_6)}{2} & 0 & 1 & -1 \\ 0 & 0 & 0 & 0 \end{bmatrix}.$$

To complete the above description, we can add

$$y(t) = Cx(t), \tag{2}$$

$$z(t) = Dv(t), \tag{3}$$

where C is a full-rank 3×3 matrix describing the states (or linear combinations thereof), the measurements of which are available; and D is a full-rank 4×4 matrix relating the actual value of the system inputs and the available measurements. The observation equation in (2) describes the state measurements available for feedback control, while (3) describes the state measurements available for feedforward control; both sets of measurements are key in our FDI filters.

In (1), we multiply on both sides by $E^{-1}_{\sigma(t)}$ to obtain:

$$\frac{dx(t)}{dt} = A_{\sigma(t)}x(t) + B_{\sigma(t)}v(t), \tag{4}$$

where $A_{\sigma(t)} = E^{-1}_{\sigma(t)}F_{\sigma(t)}$ and $B_{\sigma(t)} = E^{-1}_{\sigma(t)}G_{\sigma(t)}$. In order to ease the notation in subsequent developments, and without loss of generality, we assume that the three phases are symmetric and identical, i.e., $L_a = L_b = L_c = L$, and $R_a = R_b = R_c = R$. Then, the resulting matrices $A_{\sigma(t)}$ and $B_{\sigma(t)}$ are

$$A_{\sigma(t)} = \begin{bmatrix} -\frac{R}{L} & 0 & 0 \\ 0 & -\frac{R}{L} & 0 \\ 0 & 0 & -\frac{R}{L} \end{bmatrix},$$

$$B_{\sigma(t)} = \begin{bmatrix} k_1(t) & \frac{2}{3L} & -\frac{1}{3L} & -\frac{1}{3L} \\ k_2(t) & -\frac{1}{3L} & \frac{2}{3L} & -\frac{1}{3L} \\ k_3(t) & -\frac{1}{3L} & -\frac{1}{3L} & \frac{2}{3L} \end{bmatrix}, \tag{5}$$

where

$$k_1(t) = \frac{-2(s_1 - s_2) + (s_3 - s_4) + (s_5 - s_6)}{6L},$$

$$k_2(t) = \frac{(s_1 - s_2) - 2(s_3 - s_4) + (s_5 - s_6)}{6L},$$

$$k_3(t) = \frac{(s_1 - s_2) + (s_3 - s_4) - 2(s_5 - s_6)}{6L}. \tag{6}$$

2) Post-Fault System Model: Now, in the system of Fig. 1, assume the occurrence of a fault that causes the matrices $A_{\sigma(t)}$ and $B_{\sigma(t)}$ to change. For example (and without loss of generality), consider a fault in phase a that causes the resistance value R_a to change over time; this could be a gradual increase in resistance, i.e., a *soft fault*; or a sudden fault causing an open-circuit, i.e., a *hard fault*. Thus, to capture this class of faults, the value that the phase a resistance takes over time can be described by $R_a(t) = R + \Delta R_a(t)$, where R is the pre-fault (nominal) phase a resistance, and $\Delta R_a(t)$ describes the magnitude of the fault as time evolves. Then, after this fault, the system dynamics can be described by

$$\frac{dx}{dt} = \tilde{A}_{\sigma(t)}x(t) + \tilde{B}_{\sigma(t)}v(t), \tag{7}$$

where $\tilde{B}_{\sigma(t)} = B_{\sigma(t)}$, $\forall t$, and

$$\tilde{A}_{\sigma(t)} = \begin{bmatrix} -\frac{R}{L} - \frac{2\Delta R_a(t)}{3L} & 0 & 0 \\ \frac{\Delta R_a(t)}{3L} & -\frac{R}{L} & 0 \\ \frac{\Delta R_a(t)}{3L} & 0 & -\frac{R}{L} \end{bmatrix}.$$

It can be shown (see, e.g., [23]) that (7) can be written as the pre-fault dynamics in (1) plus an additional term that captures the effect of the fault on the pre-fault system dynamics:

$$\frac{dx(t)}{dt} = A_{\sigma(t)}x + B_{\sigma(t)}v(t) + \phi(t)f, \tag{8}$$

where $f = [-2, 1, 1]^T$ is referred to as the *fault signature*, and $\phi(t) = \frac{\Delta R_a(t)}{3L}i_a(t)$ is referred to as the *fault magnitude function*. In this case, although the fault magnitude is not a function of the switching signal, in general it is; this becomes apparent in the case studies presented in Sections IV and V.

A similar development follows for the case when there is a fault that affects the observation equations in (2)–(3), i.e., we can write the post-fault observation equation as the pre-fault observation equations plus an additional term that captures the effect of the fault. Thus

$$y(t) = Cx(t) + \theta(t)g, \tag{9}$$

$$z(t) = Dv(t) + \rho(t)h, \tag{10}$$

where $\theta(t)g$ and $\rho(t)h$ capture the effect of faults.

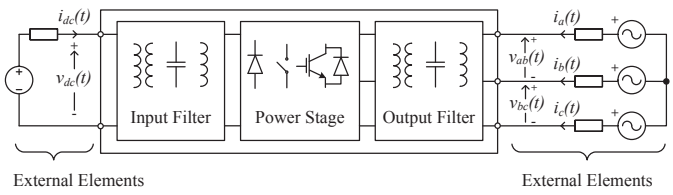

Fig. 2. AC-DC power electronics system building blocks.

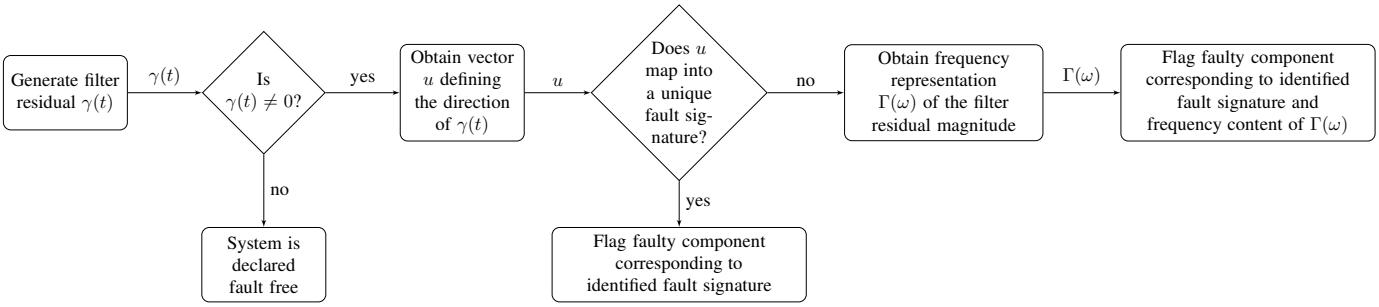

Fig. 3. Process by which detection and isolation of faults in individual components is accomplished.

B. Generalized Model for AC-DC Power Electronics Systems

In this section, we generalize the modeling ideas introduced thus far to any three-phase AC-DC power electronics system of the form in Fig. 2 that can obtained by a cascade interconnection of: i) an input filter comprised of storage elements, ii) a power stage comprised of switching devices, and iii) an output filter also comprised of storage elements. The *external elements* connected to the dc and ac ends are not considered part of the system and as such we are not concerned with detecting faults in these elements (we assume they have their own FDI mechanisms as appropriate). However, we assume that some of the interface variables that these external elements share with the AC-DC power electronics system can be measured (e.g., line-to-line voltages or phase currents on the ac end, and voltage across the terminals of the dc end). This essentially decouples the detection of faults within the AC-DC power electronics system from events affecting the external elements.

Let $x(t) \in \mathbb{R}^n$ denote the state vector, $v(t) \in \mathbb{R}^m$ the input vector, $y(t) \in \mathbb{R}^n$ the state measurements, $z(t) \in \mathbb{R}^m$ the input measurements, and $\sigma(t)$ the switching signal. Consider s different possible component faults, the j^{th} of which is described by a real-valued function $\phi_j(t)$—the fault magnitude function—, and a vector f_j—the fault signature. Similarly, we also assume that the state-measurement [input-measurement] sensors are subject to r [q] faults, each of which is captured by an additive perturbation of the form $\theta_j(t)g_j$ [$\rho_j(t)h_j$], where $\theta_j(t)$ [$\rho_j(t)$] is the fault magnitude function and g_j [h_j] is the fault signature. Then, the dynamics of an AC-DC power electronics system of the form in Fig. 2 (including the behavior in the presence of faults) can be generally described by

$$\begin{aligned}
\frac{dx(t)}{dt} &= A_{\sigma(t)}x(t) + B_{\sigma(t)}v(t) + \sum_{j=1}^{s}\phi_j(t)f_j,\\
y(t) &= Cx(t) + \sum_{j=1}^{r}\theta_j(t)g_j,\\
z(t) &= Dv(t) + \sum_{j=1}^{q}\rho_j(t)h_j,
\end{aligned} \tag{11}$$

where we impose the matrix $C \in \mathbb{R}^{n\times n}$ to be full rank, i.e., all the states (or linear combinations thereof) can be measured. This automatically ensures that the pairs $\{A_p, C\},\ p \in \mathcal{P}$, are observable, which is necessary in the development of our FDI filters. Similarly, we impose $D \in \mathbb{R}^{m\times m}$ to be also full rank.

III. Fault Detection and Isolation Filter Design

In this section, we first formulate the problem of designing an FDI filter for a three-phase AC-DC power electronics system. Then, we propose an FDI filter that uses the switched linear state-space model of the system. We also provide an estimate of the time to detection and isolation that can be achieved with our FDI filter; and compare it with the time to detection and isolation that can be achieved with other methods proposed in the literature.

A. The FDI Filter Design Problem

Consider the linear-switched system in (11); the objective is to design a causal filter that takes $z(t)$, $y(t)$, and $\sigma(t)$ as inputs and generates a residual $\gamma(t)$ with the following properties:

- P1 Whenever the system is fault-free, i.e., for all $t > 0$, $\phi_i(t)f_i = 0,\ \forall i$, $\theta_j(t)g_j = 0,\ \forall j$, and $\rho_l(t)h_l = 0,\ \forall l$, then the filter residual asymptotically converges to zero, i.e., $\lim_{t\to\infty}\gamma(t) = 0$.
- P2 When a fault occurs at time $t = t_f$ affecting $\{A_{\sigma(t)}, B_{\sigma(t)}\}$, i.e., for some j, $\phi_j(t)f_j \neq 0,\ \forall t \geq t_f$, then as $t \to \infty$, the filter residual tends to align with the vector Cf_j.
- P3 When a fault occurs at time $t = t_f$ affecting C, i.e., for some j, $\theta_j(t)g_j \neq 0,\ \forall t > t_f$, then as $t \to \infty$, the filter residual lies in a subspace spanned by $\{C(A_p + \mu I)g_j\},\ p \in \mathcal{P}$.
- P4 When a fault occurs at time $t = t_f$ affecting D, i.e., for some j, $\rho_j(t)h_j \neq 0,\ \forall t > t_f$, then as $t \to \infty$, the filter residual lies in a subspace spanned by $\{CB_pD^{-1}h_j\},\ p \in \mathcal{P}$.

Next, we introduced the notions of *fault detection* and *fault isolation* and explain how they relate to properties P1–P4; in the process, we explain the decisions and operations involved in the process of Fig. 3.

Fault detection: This is a binary decision on whether or not a fault has occurred. In this regard, it is clear from P1-P4 that by directly observing the filter residual, fault detection is straightforward, i.e., if for large enough t, we have that $\gamma(t)$ tends to 0, then the system is declared fault-free; on the other hand, we can conclude that a fault affecting a component within the system has occurred if, for all t greater than some time t_f (denoting the time at which the fault occurs), we have that $\gamma(t) \neq 0$; in Fig. 3, this binary decision is captured by the first decision block. □

Fault isolation: Once a fault has been detected, fault isolation entails determining the location of the component where the fault originated. A key observation that can be inferred from P1-P4 is that, if each fault has a unique signature, it is possible to isolate a fault by direct observation of the filter residual direction; in Fig. 3, this is captured by the second decision block. On the other hand, if there are several faults with the same signature, by just inspecting the filter residual direction we cannot distinguish them apart; in this case, as shown in Fig. 3, the residual magnitude frequency spectrum provides additional information that can be used for isolation (this idea is illustrated in Section IV-B4). □

B. Solution to the FDI Filter Design Problem

In order to solve the FDI filter design problem, we propose a causal filter of the form

$$\begin{aligned}\frac{d\hat{x}(t)}{dt} &= A_{\sigma(t)}\hat{x} + B_{\sigma(t)}D^{-1}z(t) + L_{\sigma(t)}\gamma(t),\\ \gamma(t) &= y(t) - C\hat{x}(t).\end{aligned} \tag{12}$$

where $\sigma(t)$, $A_{\sigma(t)}$, $B_{\sigma(t)}$, $p \in \mathcal{P}$ and C as in (11); and

$$L_{\sigma(t)} = \left[\mu I_n + A_{\sigma(t)}\right] C^{-1},\ \forall t, \tag{13}$$

for some $\mu > 0$ (I_n denotes the $n \times n$ identity matrix). Next, we establish that with the choice of $L_{\sigma(t)}$'s in (13), the FDI filter in (12) is stable and satisfies properties P1–P4.

1) Residual dynamics in the absence of faults: In this case, for all $t > 0$, in (11) we have that $\phi_j(t)f_j = 0,\ \forall j$. Let $e(t) := x(t) - \hat{x}(t)$, then by subtracting (12) from (11), we obtain that

$$\frac{de(t)}{dt} = \left[A - L_{\sigma(t)}C\right] e(t),$$

but with the choice of $L_{\sigma(t)}$ in (13), we have that

$$\begin{aligned}\frac{de(t)}{dt} &= -\mu e(t),\\ \gamma(t) &= Ce(t),\end{aligned}$$

for some $\mu > 0$, from where we obtain that $\lim_{t\to\infty}\gamma(t) = 0$, thus property P1 is satisfied.

2) Residual dynamics for faults affecting $\{A_\sigma(t), B_\sigma(t)\}$: In this case, we assume that for some $t = t_f$, the j^{th} fault affecting $A_{\sigma(t)}$ and/or $B_{\sigma(t)}$ manifests, i.e., $\phi_j(t)f_j \neq 0,\ \forall t \geq t_f$. By subtracting (12) from (11), we obtain that

$$\begin{aligned}\frac{de(t)}{dt} &= -\mu e(t) + \phi_j(t)f_j,\\ \gamma(t) &= Ce(t),\end{aligned}$$

thus,

$$\gamma(t) = Ce^{-\mu t}e(0) + \alpha_j(t)Cf_j, \tag{14}$$

with

$$\alpha_j(t) = \int_0^t e^{-\mu(t-\tau)}\phi_j(\tau)d\tau. \tag{15}$$

Now, since $\alpha_j(t)$ is a scalar, and the first term on the right-hand side of (14) vanishes as $t \to \infty$, it follows that, the filter residual $\gamma(t)$ will align with Cf_j as $t \to \infty$, thus property P2 is satisfied.

3) Residual dynamics for faults affecting C: In this case, for some $t = t_f$, the j^{th} fault affecting C manifests, i.e., $\theta_j(t)g_j = 0,\ \forall t \geq t_f$. By subtracting (12) from (11), we obtain that

$$\begin{aligned}\frac{de(t)}{dt} &= -\mu e(t) - \theta_j(t)(A_{\sigma(t)} + \mu I)g_j,\\ \gamma(t) &= Ce(t).\end{aligned}$$

Let $\{t_k\},\ k = 1, 2, \ldots, n$, with $t_1 \geq 0$ and $t_n \leq t$, be the sequence of switching instants in $[0, t)$, then

$$\gamma(t) = Ce^{-\mu t}e(0) + \sum_{i=0}^{n}\beta_j(t_i)C(A_{\sigma(t_i)} + \mu I)g_j, \tag{16}$$

where

$$\beta_j(t_i) = -\int_{t_i}^{t_{i+1}} e^{-\mu(t-\tau)}\theta_j(t)d\tau, \tag{17}$$

with $t_0 = 0$ and $t_{n+1} = t$. Let $\{t_{k_p}\}$ denote a subsequence of $\{t_k\}$ that corresponds to the times when mode $p \in \mathcal{P}$ is activated. Then, we can rearrange the summation term in (16) to obtain

$$\gamma(t) = Ce^{-\mu t}e(0) + \sum_{p\in\mathcal{P}}\sum_{l\in\{t_{k_p}\}}\beta_j(l)C(A_p + \mu I)g_j, \tag{18}$$

Now, since the $\beta_j(l)$'s are scalars and the first term on the right-hand side of (16) vanishes as $t \to \infty$, it follows that, as $t \to \infty$, the filter residual $\gamma(t)$ will be a linear combination of $\{C(A_p + \mu I)g\},\ p \in \mathcal{P}$, thus property P3 is satisfied.

4) Residual dynamics for faults affecting D: For some $t = t_f$, the j^{th} affecting D manifests, i.e., $\rho_j(t)h_j,\ \forall t \geq t_f$. By subtracting (12) from (11), we obtain

$$\begin{aligned}\frac{de(t)}{dt} &= -\mu e(t) - \rho_j(t)B_{\sigma(t)}D^{-1}h_j,\\ \gamma(t) &= Ce(t).\end{aligned}$$

From a similar development to that in (16)–(18), we obtain

$$\gamma(t) = Ce^{-\mu t}e(0) + \sum_{i=0}^{n}\kappa_j(t_i)CB_{\sigma(t)}D^{-1}h_j,$$

with

$$\kappa_j(t_i) = -\int_{t_i}^{t_{i+1}} e^{-\mu(t-\tau)}\rho_j(t)d\tau, \tag{19}$$

and where $\{t_k\},\ k = 1, 2, \ldots, n$, with $t_1 \geq 0$ and $t_n \leq t$, is the sequence of switching instants in $[0, t)$. Then,

$$\gamma(t) = Ce^{-\mu t}e(0) + \sum_{p\in\mathcal{P}}\sum_{l\in\{t_{k_p}\}}\kappa_j(l)CB_pD^{-1}h_j, \tag{20}$$

where $\{t_{k_p}\}$ is the subsequence of $\{t_k\}$ that corresponds to the time instants when mode $p \in \mathcal{P}$ is activated. Since the $\kappa_j(l)$'s are scalars, it follows that, as $t \to \infty$, the first term on the right-hand side of (20) vanishes, and thus $\gamma(t)$ will be a linear combination of the vectors in $\{CB_pD^{-1}\},\ p \in \mathcal{P}$, which satisfies property P4.

TABLE II
COMPARISON OF TIME TO DETECTION AND ISOLATION FOR DIFFERENT METHODS PROPOSED IN THE LITERATURE.

Reference	Detection Time [s]	Isolation Time [s]
Zhang et al., 2009 [3]	$3 \cdot 10^{-6}$	$0.2 \cdot 10^{-3}$
Peuget et al., 1998 [5]	$21.7 \cdot 10^{-3}$	$21.7 \cdot 10^{-3}$
Yazdani et al., 2011 [6]	0.3	0.3
Araujo et al., 2003 [7]	$12.4 \cdot 10^{-3}$	None
Masrur et al., 2009 [8]	$19.5 \cdot 10^{-3}$	$19.5 \cdot 10^{-3}$
Proposed FDI filter	10^{-6}	$3/\mu$ to $5/\mu$ $(+\ \tau_s)$

C. Time to Detection and Isolation

In theory, the instant a fault occurs, the filter residual is no longer zero, and thus detecting the presence of a fault should be instantaneous. In practice, it takes about 1 μs as this is the integration step of the computational platform in [22], which is the one we use in the experimental setup described in Section IV-C. However, rather than just detecting the presence of a fault, we also want to isolate it, i.e., determine the location of the faulty component. As stated earlier, fault isolation can be accomplished through analysis of i) the filter residual direction, and ii) the residual magnitude frequency spectrum. For example, in (11), consider two different faults affecting $\{A_\sigma(t), B_\sigma(t)\}$, and denote them by l and m. Respectively, denote by f_l and f_m their fault signatures, and by $\phi_l(t)$ $\phi_m(t)$ their fault magnitudes. Then, assuming that C is the identity matrix, as discussed earlier, as $t \to \infty$, which happens exponentially fast at a rate μ, the filter residual aligns with f_l whenever fault l occurs, and with f_m whenever fault m occurs. Then, for $\tau_f \in (3/\mu, 5/\mu)$ s, the residual is within $1 - 5\%$ of its steady-state value, and thus we can pick the time to isolation to be $t_{FDI} = \tau_f$. On the other hand, if $f_l = f_m$, the information contained in the frequency spectrum of $\alpha_l(t)$ and $\alpha_m(t)$, as defined in (15), can be used to distinguish the two faults apart. Thus $t_{FDI} = \tau_f + \tau_s$, where τ_s is the time it takes for the processor to perform the frequency analysis of $\alpha_l(t)$ and $\alpha_m(t)$ by using, e.g., a Fast Fourier Transform algorithm.

D. Comparison with other FDI methods

Next, we compare the time to detection and isolation that can be achieved with our FDI filters, and the time to detection and isolation that can be achieved with other FDI methods in the literature for which data is available (see Table II for details). The authors in [3] proposed a fault detection method to prevent shoot through faults in paralleled voltage source inverters; by focusing on this specific fault and converter topology, fault detection can be achieved in 3 μs, while fault isolation can be achieved in 200 μs. The authors in [5], [6], [7] proposed different model-based FDI methods with detection and isolation times ranging between 10 ms and 100 ms. Finally, the authors in [8] proposed a neural-network based FDI system; the time to detection and isolation that can be accomplished with this system is on the order of 10 ms.

As discussed in Section III-C, with our proposed FDI filter, fault detection is achieved after 1 μs, and, for faults with different signatures, isolation can be achieved within $3/\mu$ s to $5/\mu$ s (additional τ_s s are required whenever two faults have the same signature). In subsequent case studies, we show experimentally and through simulation that, we can choose $\mu = 500$ s^{-1} without compromising the dynamic performance of the filter. This results in an isolation time within 6 and 10 ms, which outperforms all the methods in Table II, except for [3]. Note, however, that the method in [3] is for a very specific type of fault and converter topology, while our FDI filters provide flexibility to cover a wide ranges of topologies and faults.

TABLE III
INVERTER WITH RL LOAD: MODEL PARAMETERS

V_{dc}	R	L	R_l	L_l	μ
230 V	0.5 Ω	12 mH	47 Ω	650 μH	500 s^{-1}

IV. DESIGN AND ANALYSIS OF AN FDI FILTER FOR A THREE-PHASE INVERTER WITH RL LOAD SYSTEM

In this section, we develop an FDI filter for the three-phase inverter with RL load system shown in Fig 1. We first provide analytical expressions for all component fault signatures and associated fault magnitude functions, and, for certain faults, we also provide analytical expressions for the filter residual dynamics. We demonstrate the performance of the FDI filter via computer simulations and hardware experiments.

A. Fault Detection and Isolation Filter

Consider again the three-phase inverter with RL load system of Fig. 1, and, as before, assume that the three phases are symmetric, i.e., $L_a = L_b = L_c = L$, and $R_a = R_b = R_c = R$. Then, the pre-fault system dynamics are described by the linear-switched state space model in (2)–(4). Assume that all the system states and inputs are directly measurable, i.e., $C = I_3$ in (2), and $D = I_4$ in (3). Then following the notation in (12) and (13), an FDI filter for this system is given by

$$\begin{aligned} \frac{d\hat{x}(t)}{dt} &= A_{\sigma(t)}\hat{x} + B_{\sigma(t)}z(t) + L_{\sigma(t)}\gamma(t), \\ \gamma(t) &= y(t) - \hat{x}(t), \end{aligned} \tag{21}$$

with $y(t) = x(t) = [i_a(t), i_b(t), i_c(t)]^T$, $z(t) = v(t) = [V_{dc}, v_a(t), v_b(t), v_c(t)]^T$; $A_{\sigma(t)}$ and $B_{\sigma(t)}$ as given in (5); and

$$L_{\sigma(t)} = \begin{bmatrix} -\frac{R}{L} + \mu & 0 & 0 \\ 0 & -\frac{R}{L} + \mu & 0 \\ 0 & 0 & -\frac{R}{L} + \mu \end{bmatrix},$$

for some $\mu > 0$. In this case, it is important to note that $A_{\sigma(t)}$ and $L_{\sigma(t)}$ are constant, which simplifies the filter residual expressions.

B. Analytical and Simulation Results

Next, we analyze the filter residual dynamics for different types of faults, providing numerical simulation results for the parameter values in Table III. The simulations are performed in the MATLAB/Simulink environment using the Piece-wise Linear Electrical Circuit Simulation (PLECS) toolbox [24]. In all simulations, we implement an open-loop controller that generates sine-triangle PWM gate signals with a carrier frequency of 16 kHz.

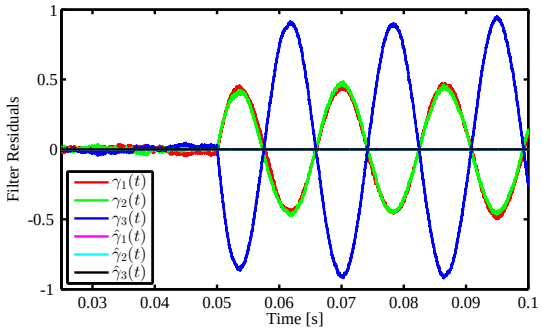

Fig. 4. Inverter with RL load: simulation of filter response for a fault causing phase c resistance to increase by $4.5\ \Omega$.

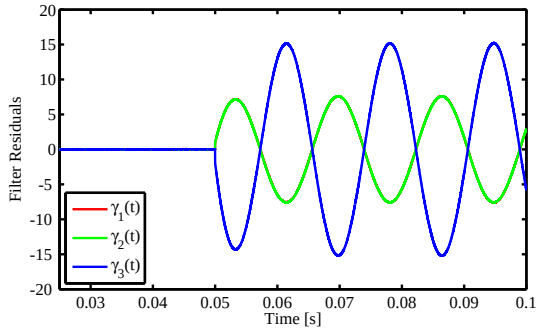

Fig. 5. Inverter with RL load: simulation of filter response for an open-circuit fault in phase c.

TABLE IV
INVERTER WITH RL LOAD: FAULT MAGNITUDE FUNCTION AND SIGNATURE FOR FAULTS CAUSING CHANGES IN THE OUTPUT FILTER PHASE RESISTANCE

i	ϕ_i(t)	f_i
1	$\frac{\Delta R_a(t)}{3L} i_a(t)$	$[-2,1,1]^T$
2	$\frac{\Delta R_b(t)}{3L} i_b(t)$	$[1,-2,1]^T$
3	$\frac{\Delta R_c(t)}{3L} i_c(t)$	$[1,1,-2]^T$

TABLE V
INVERTER WITH RL LOAD: FAULT MAGNITUDE FUNCTION AND SIGNATURE FOR FAULTS CAUSING CHANGES IN THE OUTPUT FILTER PHASE INDUCTANCE

i	ϕ_i(t)	f_i
4	$\frac{\lambda_a \Delta L_a(t) V_{dc} - 3\left(R\Delta L_a(t) - L\frac{d\Delta L_a(t)}{dt}\right) i_a(t)}{3L(3L+2\Delta L_a(t))}$	$[-2,1,1]^T$
5	$\frac{\lambda_b \Delta L_b(t) V_{dc} - 3\left(R\Delta L_b(t) - L\frac{d\Delta L_b(t)}{dt}\right) i_b(t)}{3L(3L+2\Delta L_b(t))}$	$[1,-2,1]^T$
6	$\frac{\lambda_c \Delta L_c(t) V_{dc} - 3\left(R\Delta L_c(t) - L\frac{d\Delta L_c(t)}{dt}\right) i_c(t)}{3L(3L+2\Delta L_c(t))}$	$[1,1,-2]^T$

$\sigma(t)$	1	2	3	4	5	6	7	8
λ_a	0	1	1	2	-2	-1	-1	0
λ_b	0	1	-2	-1	1	2	-1	0
λ_c	0	-2	1	-1	1	-1	2	0

1) Change in output filter phase resistance: The system dynamics for a fault causing a change in the resistance value of the output filter phase a was already derived in Section II-A2 by assuming that $R_a(t) = R + \Delta R_a(t)$, where R is the pre-fault output filter resistance, and $\Delta R_a(t)$ describes the fault magnitude as time evolves. A similar procedure can be followed to derive the system dynamics for this type of fault in phases b and c. The resulting fault magnitude functions and fault signatures are summarized in Table IV.

Now, following the notation in (14), the filter residual dynamics for a fault affecting phase c resistance is given by

$$\gamma(t) = e^{-\mu t} e(0) + \left[\int_0^t e^{-\mu(t-\tau)} \frac{\Delta R_c(t)}{3L} i_a(t) \tau \right] f_3, \quad (22)$$

with $f_3 = [1,1,-2]^T$. Now, consider that at time t_f a fault occurs causing the phase c resistance to increase by $\Delta R > 0$, i.e., $\Delta R_c(t) = \Delta R$, for all $t > t_f$. While the phase currents are not perfectly sinusoidal, the filtering effect provided by the output filter ensures that $i_c(t) \approx I \sin(\omega t)$ for some $I > 0$, then, as $t \to \infty$, it follows from (22) that

$$\gamma(t) \approx \hat{\gamma}(t) := \frac{I \Delta R}{3L} \frac{\mu \sin(\omega t) - \omega \cos(\omega t)}{\omega^2 + \mu^2} f_3. \quad (23)$$

In the simulation environment, a fault causing the phase c resistance to change according to $\Delta_{R_c}(t) = \Delta R = 4.5\ \Omega$ was injected at $t = t_f = 0.05$ s. The filter residual response $\gamma(t) = [\gamma_1(t), \gamma_2(t), \gamma_3(t)]^T$ is shown in Fig. 4, where we can see that for all $t > 0.05$ s, $\gamma(t) \neq 0$ and almost immediately after the fault occurs, the filter residual settles to a solution where $\gamma_1(t) = \gamma_2(t)$ and $\gamma_3(t) = -2\gamma_2(t)$. i.e., $\gamma(t)$ aligns with $f_3 = [1,1,-2]^T$, as expected from the analytical results in Table IV. In the same figure, we also plot $\hat{\gamma}(t) = [\hat{\gamma}_1(t), \hat{\gamma}_2(t), \hat{\gamma}_3(t)]^T$ as defined in (23). As we discuss later, the fact that the filter residual response is almost sinusoidal will play a key role in isolating this fault, i.e., distinguishing it apart from other faults with the same fault signature.

2) Output filter phase open-circuit fault: This fault can be modeled by increasing the value of the output filter phase resistance by several orders of magnitude. In this regard, on one hand, by examining $\phi_3(t) = \frac{\Delta R_c(t)}{L} i_c(t)$, which corresponds to a fault in phase c, we observe that this type of fault would result in a very large $\Delta R_c(t)$, possibly resulting in a large $\phi_3(t)$; on the other hand, $i_c(t)$ should decrease significantly, counteracting the large increase in $\Delta R_c(t)$, which would hopefully result in a reasonably small value for $\phi_3(t)$. This is indeed the case as shown in Fig. 5 by setting $\Delta R_c(t) = \Delta R = 1\ \text{M}\Omega,\ \forall t > 0.05$ s; where not only we see that the amplitude of the filter residual $\gamma(t)$ is similar to the one shown in Fig. 4, but also we see that, after the transient vanishes, the residual aligns with $f_3 = [1,1,-2]^T$. While this fault has the same fault signature as a fault causing a change in the phase resistance, the filter response is different, thus these two faults can be easily distinguished apart. In particular, by inspecting Figs. 4 and 5, we observe that the residual amplitude for the open-circuit fault is about 15 times greater than the amplitude for the resistance fault.

3) Change in output filter phase inductance: As with the output filter phase c resistance fault, this fault can be modeled by describing the phase inductance as $L_c(t) = L + \Delta L_c(t)$, where L is the pre-fault phase c inductance, and $\Delta L_c(t)$

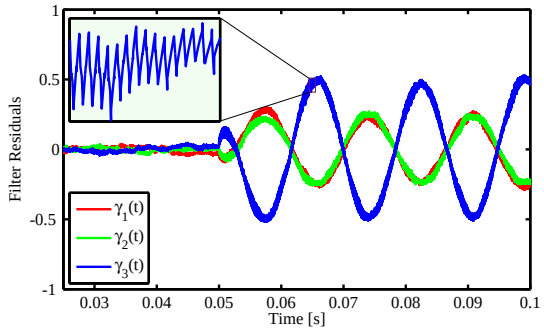

Fig. 6. Inverter with RL load: simulation of filter response for a fault causing phase c inductance to decrease by 6 mH.

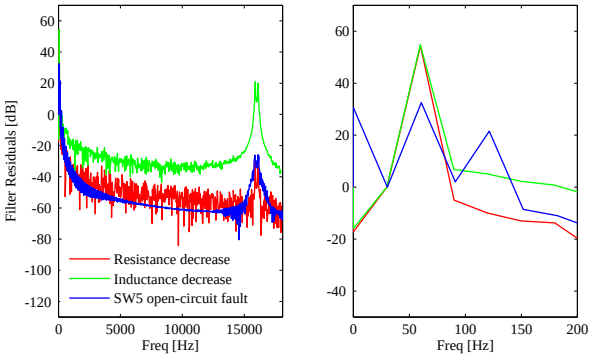

Fig. 7. Inverter with RL load: frequency analysis of the filter residual magnitude for faults phase in c.

describes the fault magnitude as time evolves. Deriving the post-fault dynamics for this case is more involved than for the resistance case as we need to manipulate terms of the form $\frac{d}{dt}\left[(L+\Delta L_c(t))i_c(t)\right]$; we omit this derivation, but provide the details of a similar one in the D-STATCOM case study presented in Section V. For all three phases, Table V presents the resulting fault magnitude functions and fault signatures.

Figure 6 shows the filter residual response $\gamma(t)$ for a fault injected at $t = t_f = 0.05$ s that causes the phase c inductance to change as $\Delta_{L_c}(t) = \Delta L = -6$ mH. Almost immediately after the fault occurs, the filter residual aligns with $f_6 = [1, 1, -2]^T$ (see Table V); however this prevents fault isolation as f_6 is equal to f_3, which corresponds to the signature of a fault that causes the output filter phase c resistance to change (see Table IV). Although we do not include the analysis results, the fault signatures of an open-circuit fault in SW_5 and SW_6 also coincide with fault signatures f_3 and f_6.

4) Fault isolation: From the analysis above, it is obvious that once the fault occurs, it can be detected as the filter residual is no longer zero. However, the fault signatures of all the components in each phase are the same, e.g., for phase c, the resistance, inductance and switches SW_5 and SW_6 (not analyzed above) have the same fault signature $[1, 1, -2]^T$, therefore by just analyzing the direction of the filter residual we can not distinguish these faults apart. A closer look at Figs. 4 and 6, corresponding to the filter residual response for faults causing, respectively, a change in phase c resistance and inductance, reveals that the fault magnitude function of these faults (see Tables IV and V) yield significantly different

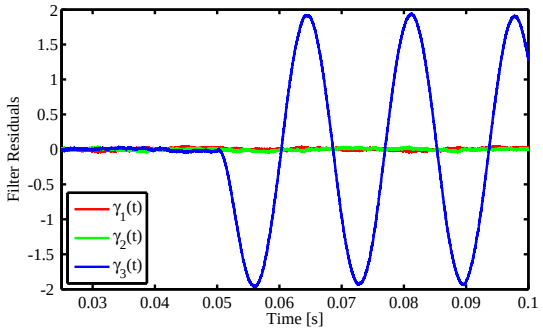

Fig. 8. Inverter with RL load: simulation of filter response for a omission fault in phase c current sensor.

TABLE VI
INVERTER WITH RL LOAD: FAULT MAGNITUDE FUNCTION AND SIGNATURE FOR FAULTS IN CURRENT SENSORS

i	$\theta_i(t)$	g_i
1	$\left(-\frac{R}{L}+\mu\right)\Delta G_a(t)\left(i_a(t)+\Delta B_a(t)\right)$	$[1,0,0]^T$
2	$\left(-\frac{R}{L}+\mu\right)\Delta G_b(t)\left(i_b(t)+\Delta B_b(t)\right)$	$[0,1,0]^T$
3	$\left(-\frac{R}{L}+\mu\right)\Delta G_c(t)\left(i_c(t)+\Delta B_c(t)\right)$	$[0,0,1]^T$

responses. In particular, the filter residual response for the resistance fault is a 60-Hz sinusoid, whereas the residual response for the inductance fault also contains higher order harmonics. Thus, a spectral analysis of the residual magnitude provides additional information to distinguish these faults apart.

Figure 7 shows the spectral analysis of the individual filter residual magnitude functions for faults in phase c causing i) the output filter resistance to decrease, ii) the output filter inductance to decrease, and iii) an open-circuit in SW_5. For the resistance fault, the spectrum is concentrated mostly around 60 Hz, with a small double peak around the switching frequency. The spectrum for the inductor shares some features with the spectrum of the resistor fault; however, the peak near the switching frequency is much larger ($\sim$ 30 dB) than for the resistance fault due to the dependence of the filter residual on the switching signal. Thus, this peak near the switching frequency can be used to distinguish this fault apart from the resistance fault. For an open-circuit in SW_5, the 60-Hz component and the peak around the switching frequency are similar to the ones for the inductance fault, but there are two additional components at 0 Hz and 120 Hz. Thus, these two additional frequency components can be used to distinguish apart inductance and switch open-circuit faults.

5) Current sensor fault: Consider the current sensor of phase c; a fault in this sensor can be modeled by describing the corresponding observation equation as $y_3 = [1 + \Delta G_c(t)]x_3(t) + \Delta B_c(t)$, where $x_3(t) = i_c(t)$ and $\Delta G_c(t)$, $\Delta B_c(t)$, respectively, describe the effect of a fault that causes a change in the sensor gain and a measurement bias. Table VI presents the resulting fault magnitude function and fault signature (it also collects the corresponding counterparts for faults in the current sensors of the other two phases).

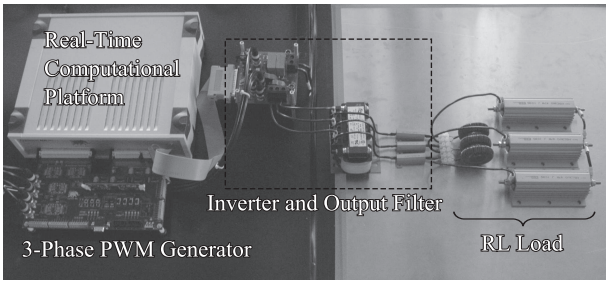

Fig. 9. Experimental testbed main building blocks.

TABLE VII
EXPERIMENTAL TESTBED: SPECIFICATIONS OF MAIN BUILDING BLOCKS

DC power supply ratings	300 V, 16 A, 5 kW
Inverter module ratings	20 A, 600 V
Output filter	
Resistance, per phase	0.5 Ω
Inductance, per phase	12 mH
RL load	
Resistance, per phase	23.5 Ω, 47 Ω (nominal), 67 Ω, 94 Ω
Inductance, per phase	650 μH
Current sensors bandwidth	200 kHz
PWM generator	
Switching frequency	4 kHz
Dead time	1 μs
Volts / freq. scalar	3.83
Real-time platform	
FPGA device	Xilinx Virtex-5 ML506
Clock speed	100 MHz
ADC sapling rate	1 MSPS
DAC sampling rate	1 MSPS

As stated in property P4, when a fault in the phase c current sensor occurs, as $t \to \infty$, the filter residual should lie in the subspace spanned spanned by $\{C(A_p + \mu I)g_3\}, p \in \mathcal{P}$. However, for this particular system, the filter residual aligns with $g_3 = [0, 0, 1]^T$; this is the case because $C = I_3$ and $A_{\sigma(t)}$ is diagonal. Figure 8 shows the filter residual response $\gamma(t)$ for a so-called omission fault in the current sensor of phase c, i.e., $\Delta G(t) = -1$, for all $t > t_f$, where $t_f = 0.05$ s, and $\Delta B(t) = 0$, $\forall t$. As expected, almost immediately after the fault, the residual aligns with $g_3 = [0, 0, 1]^T$.

C. Experimental Results

In order to experimentally demonstrate the feasibility of the proposed filter for FDI in the system of Fig. 1, we developed the experimental testbed shown in Fig. 9. All three phase currents and voltages are measured and passed to the FDI filter residual generator, which is implemented in a FPGA-based platform, running on a real-time processor in lockstep with the physical system. Additionally, we have a mechanism to artificially inject certain faults into the physical system; for each of these faults, we compare the resulting filter residual response with that obtained with the simulation-based model. Table VII provides the specifications of the main building blocks that comprise the experimental testbed.

1) FDI filter implementation: As time evolves, to execute the FDI filter in lockstep with the physical system, we use the generalized automaton modeling approach described in [22], which, among other things, enables the implementation of the linear-switched state-space model in (12)–(13) that defines the FDI filter. During real-time execution, a direct memory indexing technique controls the selection of the active mode based on the system input $z(t)$ and boundary conditions defined by $\hat{y}(t) = C\hat{x}$. A linear solver computes the state vector $\hat{x}(t)$ and the corresponding estimated output vector $\hat{y}(t)$, and filter residual $\gamma(t)$. An internal signal generator and external analog and digital input ports provide the input vector $v(t)$ to the state-space solver. The state vector $\hat{x}(t)$ and the output vector $\hat{y}(t)$ are accessible in real-time through low-latency analog output ports. The processor architecture, which is implemented in an FPGA, guarantees the execution time for each time interval to be shorter than the fixed simulation time step. Furthermore, the loop-back latency is minimized with custom designed input-output hardware, and has been characterized to be on the order of 1 μs [22].

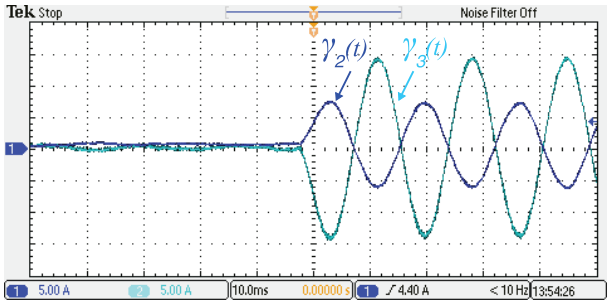

Fig. 10. Inverter with RL load: experimental filter response for an open-circuit fault in phase c.

2) Phase open-circuit fault: Figure 10 shows the real-time FDI filter residual response before and after phase c of the RL load is disconnected (so as to mimic the effect of an open-circuit fault in this phase). In this figure, we can see that after the transient vanishes, the filter residual is proportional to the vector $[1, 1, -2]^T$, which matches the fault signature f_3 analytically derived for this type of fault (see Table IV). Also, the filter residual exhibits a sinusoidal behavior, matching the simulation results in Fig. 5.

3) Current sensor fault: Figure 11 displays the real-time response of the FDI filter after the current sensor of phase c is disconnected. The filter residual matches the simulation results shown in Fig. 8. As in the simulations, after the transient vanishes, the filter residual aligns with the vector $[0, 0, 1]^T$, which matches the fault signature g_3 analytically derived for this fault (see Table VI). This provides with sufficient information to unequivocally determine that the faulty component is the current sensor of phase c.

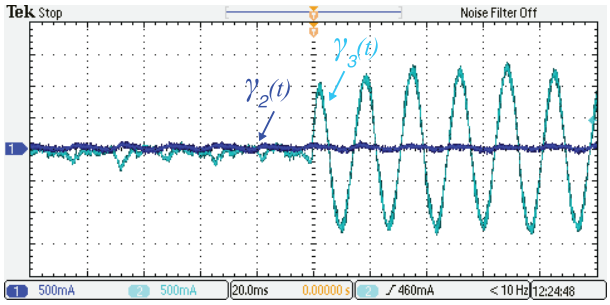

Fig. 11. Inverter with RL load: experimental filter response for an omission fault in phase c current sensor.

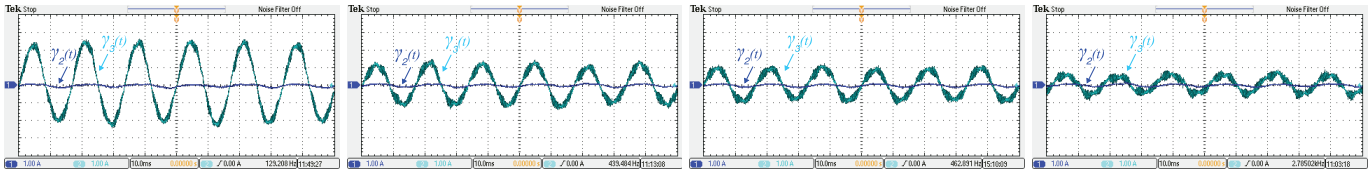

(a) $R_l = 23.5\ \Omega$. (b) $R_l = 47\ \Omega$. (c) $R_l = 67\ \Omega$. (d) $R_l = 94\ \Omega$.

Fig. 12. Inverter with RL load: filter response for different values of R_l and a fault in phase c current sensor. [Scope settings are 1 A/div and 10 ms/div.]

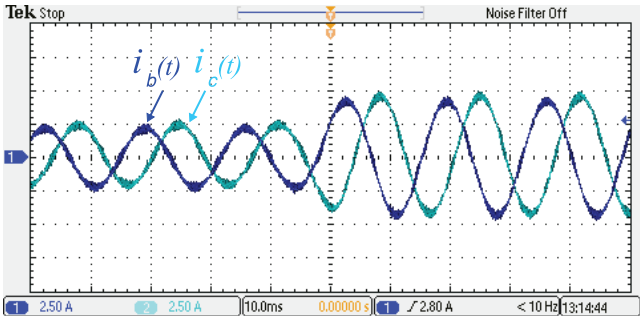

(a) Phase currents.

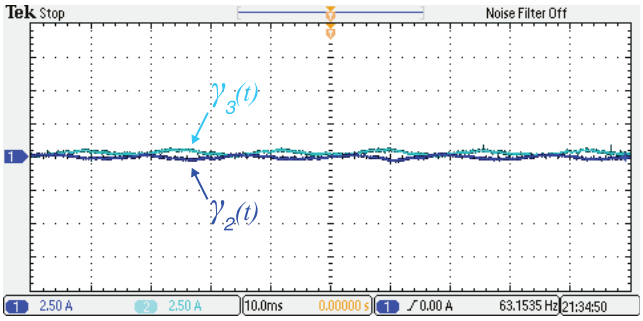

(b) Filter residual response.

Fig. 13. Inverter with RL load: experimental filter response for a load variation that results in R_l to decrease by 50% of its nominal value.

4) Effect of different load parameter values: For the same fault in the current sensor of phase c discussed above, Fig. 12 displays the FDI filter response when the load resistance takes the following values: $R_l = 23.5\ \Omega$, $R_l = 47\ \Omega$ (nominal), $R_l = 67\ \Omega$, and $R_l = 94\ \Omega$. As it can be seen in this figure, the filter residual magnitude depends on the value that R_l takes and, in general, the larger R_l is, the smaller the residual magnitude is. However, it is important to note that, independently of the value of R_l, the filter residual aligns with the vector $[0, 0, 1]^T$; this provides with enough information to conclude that the faulty component is the current sensor of phase c.

5) Effect of load variations: Finally, we discuss the effect of load variations on the filter performance. As discussed in Section II-B, the RL load is considered an external element to the system being monitored (in this case, comprised of a power stage and an output filter). Thus, events that affect this external element should not be flagged by the FDI filter. To illustrate this, consider a load variation that results in the load resistance changing from $R_l = 47\ \Omega$ to $R_l = 23.5\ \Omega$. Figure 13(a) shows the sudden change in phase currents when the load changes. Figure 13(b) displays the corresponding filter residual evolution; as expected, this event is not flagged as a fault.

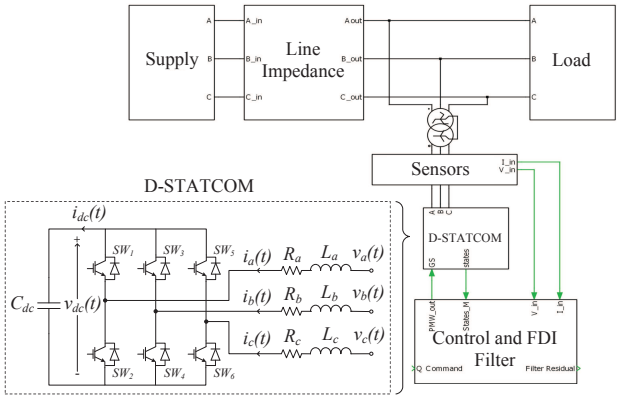

Fig. 14. D-STATCOM Simulation Block Diagram.

V. Design and Analysis of an FDI Filter for a D-STATCOM

In this section, we develop an FDI filter for a D-STATCOM [Distributed Static Compensator]. A D-STATCOM is a distribution-level controller that is often tied to highly nonlinear loads to reduce their disturbance to the grid, or to loads that require very strict power quality control [25], [26]. The most basic D-STATCOM consists of a voltage source converter tied to a capacitor on the dc end, and tied to a filter on the ac end (see Fig. 14).

A. Pre-Fault Dynamics and FDI Filter

Consider the circuit at the bottom left of Fig. 14, and assume that $L_a = L_b = L_c = L$, and $R_a = R_b = R_c = R$. Let $s_i(t)$, $i = 1, 2, \ldots, 6$, be an indicator variable that, at time t, takes value 0 whenever SW_i is open, and 1 whenever is closed. Then, the pre-fault circuit dynamics are described by

$$\begin{aligned} \frac{d}{dt}x(t) &= A_{\sigma(t)}x(t) + B_{\sigma(t)}v(t), \\ y(t) &= Cx(t), \\ z(t) &= Dv(t), \end{aligned} \tag{24}$$

where $x(t) = [i_a(t), i_b(t), i_c(t), v_{dc}(t)]^T$, $v(t) = [v_a(t), v_b(t), v_c(t)]^T$, $C = I_4$, $D = I_3$, and

$$A_{\sigma(t)} = \begin{bmatrix} -\frac{R}{L} & 0 & 0 & k_{1(t)} \\ 0 & -\frac{R}{L} & 0 & k_2(t) \\ 0 & 0 & -\frac{R}{L} & k_3(t) \\ k_4(t) & k_5(t) & k_6(t) & k_7(t) \end{bmatrix},$$

$$B_{\sigma(t)} = \begin{bmatrix} \frac{2}{3L} & -\frac{1}{3L} & -\frac{1}{3L} \\ -\frac{1}{3L} & \frac{2}{3L} & -\frac{1}{3L} \\ -\frac{1}{3L} & -\frac{1}{3L} & \frac{2}{3L} \\ 0 & 0 & 0 \end{bmatrix}, \tag{25}$$

with

$$k_1(t) = \frac{-2(s_1 - s_2) + (s_3 - s_4) + (s_5 - s_6)}{6L},$$
$$k_2(t) = \frac{(s_1 - s_2) - 2(s_3 - s_4) + (s_5 - s_6)}{6L},$$
$$k_3(t) = \frac{(s_1 - s_2) + (s_3 - s_4) - 2(s_5 - s_6)}{6L},$$
$$k_4(t) = \frac{s_1 - s_2}{C_{dc}}, \quad k_5(t) = \frac{s_3 - s_4}{C_{dc}},$$
$$k_6(t) = \frac{s_5 - s_6}{C_{dc}}, \quad k_7(t) = 0, \tag{26}$$

where the possible open/closed switch combination are the same as for the inverter with RL load system (see Table I).

Now, following the same notation as in (12) and (13), an FDI filter for this system is given by

$$\frac{d\hat{x}(t)}{dt} = A_{\sigma(t)}\hat{x} + B_{\sigma(t)}z(t) + L_{\sigma(t)}\gamma(t),$$
$$\gamma(t) = y(t) - \hat{x}(t), \tag{27}$$

with $y(t) = x(t)$, $z(t) = v(t)$; $A_{\sigma(t)}$ and $B_{\sigma(t)}$ as in (25); and

$$L_{\sigma(t)} = \begin{bmatrix} -\frac{R}{L} + \mu & 0 & 0 & k_{1(t)} \\ 0 & -\frac{R}{L} + \mu & 0 & k_2(t) \\ 0 & 0 & -\frac{R}{L} + \mu & k_3(t) \\ k_4(t) & k_5(t) & k_6(t) & \mu \end{bmatrix},$$

for some $\mu > 0$. In this case, it is important to note that, unlike in the inverter with RL load system, the matrices $A_{\sigma(t)}$ and $L_{\sigma(t)}$ depend on the switching signal, which complicates the detection and isolation of faults affecting C (see property P3). On the other hand, since $B_{\sigma(t)}$ is constant, the detection of faults affecting D simplifies significantly (see property P4).

B. Analytical and Simulation Results

Next, we analyze the filter residual dynamics for different types of faults, providing numerical simulation results for the parameter values in Table VIII; the simulations are performed in MATLAB/Simulink/PLECS. Figure 14 provides a block diagram of the simulation model; the *supply* block is comprised of a three-phase ideal voltage source, the *line impedance* block is a series-connection of inductors and resistors, whereas the *load* block is comprised of inductive reactances. The controller is adapted from the voltage-mode controller in [27]. This controller includes a phase-lock loop that generates sine-triangle PWM gate signals with a carrier frequency of 5 kHz.

1) Change in dc end capacitance: In order to capture the effect of this fault, we describe the capacitance as $C_{dc}(t) = C_{dc} + \Delta C_{dc}(t)$, where C_{dc} is the pre-fault capacitance value

TABLE VIII
D-STATCOM MODEL PARAMETERS

V_{ac}	R	L	C_{dc}	μ
480 V	0.1 Ω	10 mH	2 mF	500 s^{-1}

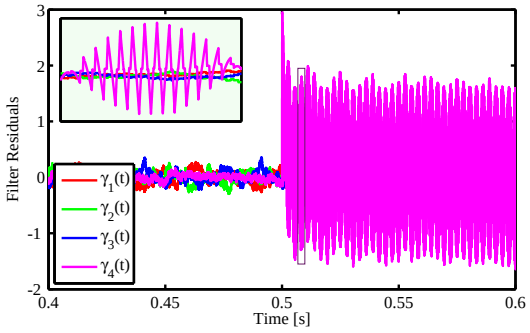

Fig. 15. D-STATCOM: simulation of filter response for 50% decrease in dc end capacitance.

TABLE IX
D-STATCOM: FAULT MAGNITUDE FUNCTION AND SIGNATURE FOR FAULTS IN DC END CAPACITOR

$\phi_1(t)$	f_1
$\lambda\frac{\Delta C_{dc}(t) i_{dc} - C\frac{d\Delta C_{dc}(t)}{dt} v_{dc}}{C_{dc}[C_{dc}+\Delta C_{dc}(t)]}$	$[0,0,0,1]^T$

$\sigma(t)$	1	2	3	4	5	6	7	8
i_{dc}	0	i_c	i_b	i_a	i_a	i_b	i_c	0
λ	0	-1	-1	1	-1	1	1	0

and $\Delta C_{dc}(t)$ describes the change in capacitance due to the fault. Thus, the relation between the dc end voltage and current is given by $\frac{d}{dt}[C_{dc} + \Delta C_{dc}(t)]v_{dc} = i_{dc}(t)$, from where it follows that

$$\frac{dv_{dc}(t)}{dt} = \frac{1}{C_{dc} + \Delta C_{dc}(t)}\left(i_{dc}(t) - \frac{d\Delta C_{dc}(t)}{dt} v_{dc}(t)\right);$$

therefore, the post fault dynamics can be described by

$$\frac{dx(t)}{dt} = \tilde{A}_{\sigma(t)}x(t) + \tilde{B}_{\sigma(t)}v(t), \tag{28}$$

with $\tilde{B}_{\sigma(t)} = B_{\sigma(t)}$, and

$$\tilde{A}_{\sigma(t)} = \begin{bmatrix} -\frac{R}{L} & 0 & 0 & k_1(t) \\ 0 & -\frac{R}{L} & 0 & k_2(t) \\ 0 & 0 & -\frac{R}{L} & k_3(t) \\ \tilde{k}_4(t) & \tilde{k}_5(t) & \tilde{k}_6(t) & \tilde{k}_7(t) \end{bmatrix}, \tag{29}$$

where $k_1(t)$–$k_3(t)$ are the same as in (26), and

$$\tilde{k}_4(t) = \frac{s_1 - s_2}{C_{dc} + \Delta C_{dc}(t)},$$
$$\tilde{k}_5(t) = \frac{s_3 - s_4}{C_{dc} + \Delta C_{dc}(t)},$$
$$\tilde{k}_6(t) = \frac{s_5 - s_6}{C_{dc} + \Delta C_{dc}(t)},$$
$$\tilde{k}_7(t) = -\frac{\frac{d}{dt}\Delta C_{dc}(t)}{C_{dc} + \Delta C_{dc}(t)}. \tag{30}$$

Now, by rearranging (29) as in (8), we obtain the fault signature f_1, and the fault magnitude function $\phi_1(t)$, both of which are given in Table IX.

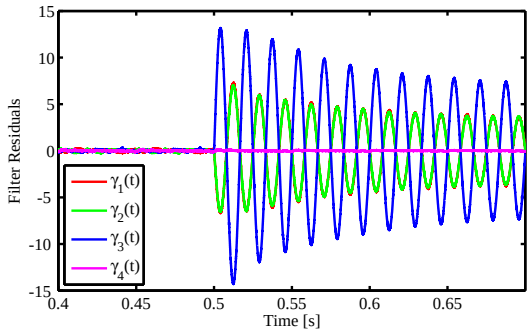

Fig. 16. D-STATCOM: simulation of filter response for a fault causing phase c resistance to change from 0.1 Ω to 0.5 Ω.

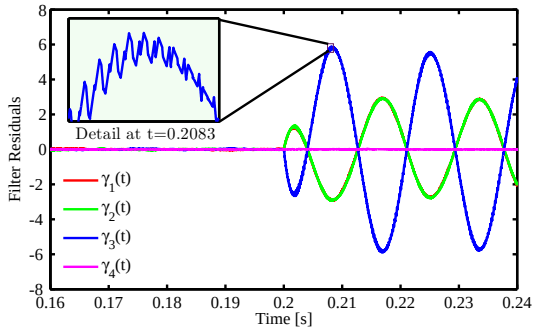

Fig. 17. D-STATCOM: simulation of filter response for a fault causing the output filter phase c inductance to change from 10 mH to 5 mH.

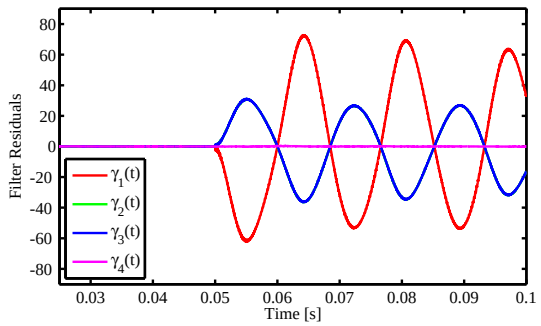

Fig. 18. D-STATCOM: simulation of filter response for a short-circuit fault between the node connecting switches SW_1 and SW_2 and ground.

TABLE X
D-STATCOM: FAULT MAGNITUDE FUNCTION AND SIGNATURE FOR SWITCH OPEN-CIRCUIT FAULTS

Fault	ϕ_i(t)	f_i
SW_1 $(i=8)$	$\frac{-v_{dc}(t)(s_4+s_6)-3Ri_a(t)}{6}$	$[-2,1,1,0]^T$
SW_2 $(i=9)$	$\frac{v_{dc}(t)(s_3+s_5)-3Ri_a(t)}{6}$	$[-2,1,1,0]^T$
SW_3 $(i=10)$	$\frac{-v_{dc}(t)(s_2+s_6)-3Ri_b(t)}{6}$	$[1,-2,1,0]^T$
SW_4 $(i=11)$	$\frac{v_{dc}(t)(s_1+s_5)-3Ri_b(t)}{6}$	$[1,-2,1,0]^T$
SW_5 $(i=12)$	$\frac{-v_{dc}(t)(s_2+s_4)-3Ri_c(t)}{6}$	$[1,1,-2,0]^T$
SW_6 $(i=13)$	$\frac{v_{dc}(t)(s_1+s_3)-3Ri_c(t)}{6}$	$[1,1,-2,0]^T$

Figure 15 shows the filter residual response for a fault injected at $t_f = 0.5$ s causing a decrease of 50% in the dc end capacitance. As expected, after the initial transient vanishes, the filter residual aligns with $f_1 = [0,0,0,1]^T$.

2) Change in output filter phase resistance: For this type of fault, it is clear from (25) that only the equations for the phase currents will be altered; in fact the derivation of the post-fault model is very similar to the one for the inverter with RL load model derived in Section II-A2; thus, we omit it. Therefore, the fault magnitude functions $\phi_i(t)$, $i = 2,3,4$, are the same as the corresponding ones in Table IV; however the fault signatures are 4-dimensional vectors, respectively denoted by f_2, f_3, f_4, instead of 3-dimensional ones. In particular the first three entries of each f_i, $i = 2,3,4$, coincide with the entries of the corresponding fault signature vectors in Table IV; while the fourth entry is equal to zero for all f_i's, e.g., $f_2 = [-2,1,1,0]^T$. In the simulation environment, a fault causing the resistance of phase c to change from 0.1 Ω to 0.5 Ω is injected at $t_f = 0.5$ s; Fig. 16 shows the evolution of the filter residual. After the transient vanishes, the filter residual aligns with $f_4 = [1,1,-2,0]^T$, as expected.

3) Change in output filter phase inductance: Similarly as for faults causing changes in phase resistance, from (25), it is easy to see that a fault causing the phase inductance to change will only affect the current equations, with a post-fault model similar to the one for the inverter with RL load system. Then, the fault magnitude functions for phase a, b, and c inductors, denoted respectively by $\phi_5(t)$, $\phi_6(t)$, and $\phi_7(t)$ are the same as those for the inverter with RL system given in Table V. The corresponding fault signature vectors, respectively denoted by f_5, f_6, f_7, are 4-dimensional. Specifically, the first three entries of each f_i are equal to the entries of the corresponding fault signature vectors in Table V, while the fourth entry is equal to zero, e.g., $f_5 = [-2,1,1,0]^T$. Figure 17 shows the filter residual evolution for a fault that causes the inductance of phase c to change from 10 mH to 5 mH; as expected, when the filter residual reaches steady state, it aligns with $f_7 = [1,1,-2,0]^T$.

4) Other faults: Table X shows the fault magnitude functions and fault signatures for switch open-circuit faults; the ones for sensor faults are similar to the corresponding ones for the inverter with RL load system and are therefore omitted.

As with the inverter with RL load system, the fault signatures for all the components in the same phase are identical; these include, e.g., phase-to-ground faults. For instance, a fault causing a short circuit between the node connecting switches SW_1 and SW_2 and the (grounded) neutral point of the transformer winding on the D-STATCOM side is equivalent to both phase a resistance and inductance values suddenly dropping to zero; this is consistent with the simulation results in Fig. 18 that show the evolution of the filter residual for such a phase-to-ground fault. Thus, to distinguish such a fault from other faults that affect phase a, e.g., a slight increase in phase a resistance, it is necessary to analyze the residual magnitude frequency spectrum, which yields similar results to those reported in Section IV-B4. Similarly, faults affecting both switches in the same leg, SW_1 and SW_2, SW_3 and SW_4, or SW_5 and SW_6 are equivalent to faults that cause the dc end capacitance to drop to zero suddenly.

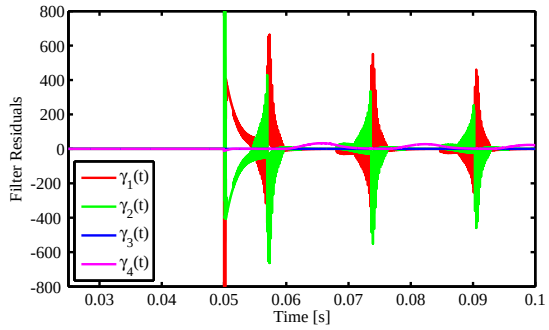

Fig. 19. D-STATCOM: simulation of filter response for a short-circuit fault between the nodes connecting SW_1 and SW_2, and SW_3 and SW_4.

Next, we discuss the performance of the filter residual for a phase-to-phase fault; in particular, we analyze a short-circuit fault between the node connecting $SW1$ and $SW2$, and the node connecting $SW3$ and $SW4$. Figure 19 displays the corresponding filter residual response, where we can see that $\gamma_1(t) = -\gamma_2(t)$ for all t after the fault occurrence, i.e., for all $t > 0.05$ s. Additionally, even if not identically equal to zero, the maximum values that $\gamma_3(t)$ and $\gamma_4(t)$ take after the fault occurrence are very small relative to those that $\gamma_1(t)$ and $\gamma_2(t)$ take. These features of the residual response, which are substantially different from those of faults previously analyzed, enable distinguishing the occurrence of this type of fault from the occurrence of all other types analyzed earlier.

5) Faults in external elements: Finally, we discuss the effect of disturbance events affecting elements external to the D-STATCOM; in the block diagram of Fig. 14, these external elements are the supply, the line impedance, and the load. Detection of faults in these elements is important from the point of view of ensuring a reliable energy delivery to the load; however, the focus here is to monitor the occurrence of faults in the components of the D-STATCOM. As such, the FDI filter should not flag as a fault any disturbance that may affect these external elements—these elements should have their own dedicated FDI mechanisms. With respect to this, we consider a voltage sag in phase a of the supply occurring at $t = 0.2$ s (see Fig. 20(a)); the corresponding filter residual evolution is displayed in Fig. 20(b). As expected, the filter residual does not change after this event occurs because this event does not correspond to a component fault within the D-STATCOM, and therefore it is not flagged as such.

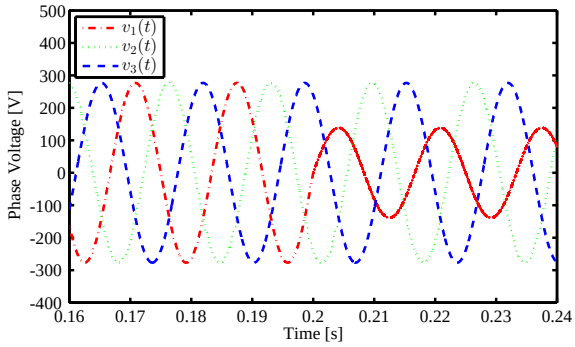

(a) Supply phase voltages.

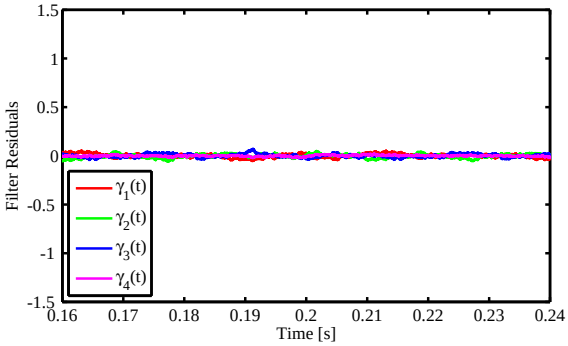

(b) Filter residual.

Fig. 20. D-STATCOM: filter response for a voltage sag on phase a.

VI. Concluding Remarks

In this paper, we proposed a new class of FDI filters for AC-DC power electronics systems. The proposed detection filters offer a model-based approach to power electronics FDI that is much faster than other techniques in the literature. Simulation and experimental results show that the proposed FDI filters are able to capture a wide range of faults and that the filter residual magnitude provides good estimates for degradation in system components. The analysis also shows that even in the case of several faults having the same fault signature (thus the direction of the filter residual is not sufficient to distinguish them apart), it is still possible to achieve isolation by analyzing the frequency spectrum of the residual magnitude.

We show the practical viability of the proposed FDI filters by i) implementing them on an application-specific real-time power electronics emulation processor architecture with 1 μs time step and loopback latency, and ii) testing their performance on a physical system. Not only these experiments confirm the practical viability of the proposed filters, but they pave the way towards high-performance, low-latency, high-speed, and inexpensive control platforms for linear-switched systems.

While the analysis, simulations and experiments in this paper are mostly focused on three-phase two-level inverters and D-STATCOM systems, the approach is general and can be easily adapted to any power electronics system that can be described by a linear-switched state-space model.

References

[1] J. Laprie, *Dependability: Basic Concepts and Terminology*. New York, NY: Springer-Verlag, 1991.

[2] R. J. Patton, P. M. Frank, and R. N. Clarke, Eds., *Fault diagnosis in dynamic systems: theory and application*. Upper Saddle River, NJ, USA: Prentice-Hall, Inc., 1989.

[3] D. Zhang, F. Wang, R. Burgos, J. Kern, S. El-Barbari, and D. Boroyevich, "Internal fault detection and isolation for paralleled voltage source converters," in *Proc. of IEEE Applied Power Electronics Conference and Exposition*, Washington, DC, 2009.

[4] K. Levin, E. Hope, and A. Domínguez-García, "Observer-based fault diagnosis of power electronics systems," in *Proceedings of IEEE Energy Conversion Congress and Exposition*, Atlanta, GA, 2010.

[5] R. Peuget, S. Courtine, and J.-P. Rognon, "Fault detection and isolation on a pwm inverter by knowledge-based model," *IEEE Transactions on Industry Applications*, vol. 34, no. 6, pp. 1318 –1326, Nov/Dec. 1998.

[6] A. Yazdani, H. Sepahvand, M. Crow, and M. Ferdowsi, "Fault detection and mitigation in multilevel converter statcoms," *IEEE Transactions on Industrial Electronics*, vol. 58, no. 4, pp. 1307–1315, Apr. 2011.

[7] R. de Araujo Ribeiro, C. Jacobina, E. da Silva, and A. Lima, "Fault detection of open-switch damage in voltage-fed pwm motor drive systems," *IEEE Transactions on Power Electronics*, vol. 18, no. 2, pp. 587 – 593, Mar. 2003.

[8] M. Abul Masrur, Z. Chen, and Y. Murphey, "Intelligent diagnosis of open and short circuit faults in electric drive inverters for real-time applications," *IET Power Electronics*, vol. 3, no. 2, pp. 279 –291, Mar. 2010.

[9] S. Khomfoi and L. Tolbert, "Fault diagnostic system for a multilevel inverter using a neural network," *IEEE Transactions on Power Electronics*, vol. 22, no. 3, pp. 1062–1069, May 2007.

[10] M. Abul Masrur, Z. Chen, and Y. Murphey, "Intelligent diagnosis of open and short circuit faults in electric drive inverters for real-time applications," *IET Power Electronics*, vol. 3, no. 2, pp. 279 –291, Mar. 2010.

[11] F. Chowdhury and J. Aravena, "A modular methodology for fast fault detection and classification in power systems," *IEEE Transactions on Control Systems Technology*, vol. 6, no. 5, pp. 623–634, Sep. 1998.

[12] C. Turpin, P. Baudesson, F. Richardeau, F. Forest, and T. Meynard, "Fault management of multicell converters," *IEEE Transactions on Industrial Electronics*, vol. 49, no. 5, pp. 988–997, 2002.

[13] R. Beard, "Failure accommodation in linear systems through self-reorganization," Man Vehicle Laboratory, Massachusetts Institute of Technology, Cambridge, MA, Tech. Rep. MVT-71-1, 1971.

[14] H. Jones, "Failure detection in linear systems," Ph.D. dissertation, Massachusetts Institute of Technology, Cambridge, MA, 1973.

[15] Z. Mihajlovic, B. Lehman, and C. Sun, "Output ripple analysis of switching DC-DC converters," *IEEE Transactions on Circuits and Systems I: Regular Papers*, vol. 51, no. 8, pp. 1596–1611, Aug. 2004.

[16] E. Hope, X. Jiang, and A. Dominguez-Garcia, "A reachability-based method for large-signal behavior verification of dc-dc converters," *IEEE Transactions on Circuits and Systems I: Regular Papers*, vol. 58, no. 12, pp. 2944–2955, Dec. 2011.

[17] D. Luenberger, Ed., *Introduction to Dynamic Systems*. New York, NY: John Wiley, 1979.

[18] J. Kassakian, M. Schlecht, and G. Verghese, *Principles of Power Electronics*. Reading, MA: Addison-Wesley, 1991.

[19] J. Mahdavi, A. Emaadi, M. Bellar, and M. Ehsani, "Analysis of power electronic converters using the generalized state-space averaging approach," *IEEE Transactions on Circuits and Systems I: Fundamental Theory and Applications*, vol. 44, no. 8, pp. 767 –770, Aug 1997.

[20] A. Alessandri and P. Coletta, "Design of Luenberger observers for a class of hybrid linear systems," in *Proc. Hybrid Systems Computation and Control*, Genova, Italy, 2001.

[21] D. Liberzon, *Switching in Systems and Control*. Boston, MA: Birkhauser, 2003.

[22] D. Majstorovic, I. Celanovic, N. Teslic, N. Celanovic, and V. Katic, "Ultra-low latency hardware-in-the-loop platform for rapid validation of power electronics designs," *IEEE Transactions on Industrial Electronics*, to appear.

[23] A. Tanwani, A. Dominguez-Garcia, and D. Liberzon, "An inversion-based approach to fault detection and isolation in switching electrical networks," *IEEE Transactions on Control Systems Technology*, vol. 19, no. 5, pp. 1059 –1074, Sep. 2011.

[24] J. Alimeling and W. Hammer, "Plecs-piece-wise linear electrical circuit simulation for simulink," in *Proc. of IEEE International Conference on Power Electronics and Drive Systems*, 1999.

[25] T. Manmek, C. Mudannayake, and C. Grantham, "Voltage dip detection based on an efficient least squares algorithm for d-statcom application," in *Proc. of CES/IEEE Power Electronics and Motion Control Conference*, Shanghai, China, 2006.

[26] G. Reed, M. Takeda, and I. Iyoda, "Improved power quality solutions using advanced solid-state switching and static compensation technologies," in *Proc. of IEEE Power Eng. Society Winter Meeting*, New York, NY, USA, 1999.

[27] N. Hingorani and L. Gyugyi, *Understanding FACTS (Concepts and Technology of Flexible AC Transmission Systems)*. Hoboken, NJ: IEEE Press, 1999.

Xiangyu Ding (S'07) received the B.S. and M.S. degrees in Electrical and Computer Engineering from the University of Illinois at Urbana-Champaign in 2011 and 2012 respectively. His research interests are in the ares of system reliability analysis, power electronics and control. He is currently with the S&C Electric Company working on electrical system design and upgrade of renewable generation stations, data centers, and utility substations.

Jason Poon (S'11) received the B.S. degree in Electrical and Computer Engineering from Olin College of Engineering in Needham, Massachusetts in 2012. He is currently with the Institute for Soldier Nanotechnologies at the Massachusetts Institute of Technology, Cambridge. His research interests include the areas of power electronics, real-time simulation, and observers.

Ivan Čelanović (M'06) received the Diploma Engineer degree from the University of Novi Sad, Republic of Serbia, in 1998; the M.Sc. degree from Virginia Polytechnic Institute and State University in 2000, and the Sc.D. degree from the Massachusetts Institute of Technology (MIT), Cambridge in 2006, all in electrical engineering and computer science. In 2006, he joined the MIT Laboratory for Electromagnetic and Electronic Systems as a Postdoctoral Associate and in 2008, he joined the MIT Institute for Soldier Nanotechnologies where he is currently a Principal Research Scientist. In 2009 he co-founded the Typhoon HIL Inc. a venture backed Power Electronics Design and Test Automation company. Typhoon HIL develops ultra-high fidelity Hardware-in-the-Loop (HIL) real-time emulation systems for test and quality assurance of power electronics control systems. His work spans ultra-high fidelity real-time emulation of power electronics, smart grid technologies and applied controls. In addition, he is working on photonic crystals, high-temperature nano-photonics, and new solid-state heat to electricity conversion systems. Dr. Celanovic has published over 45 papers and two book chapters.

Alejandro D. Domínguez-García (S'02–M'07) is an Assistant Professor in the Department of Electrical and Computer Engineering of the University of Illinois at Urbana-Champaign, where he is affiliated with the Power and Energy Systems area. His research interests are in the areas of system reliability theory and control, and their application to electric power systems, power electronics, and embedded electronic systems for safety-critical/fault-tolerant aircraft, aerospace, and automotive applications. He received the Ph.D. degree in Electrical Engineering and Computer Science from the Massachusetts Institute of Technology, Cambridge, MA, in 2007 and the degree of Electrical Engineer from the University of Oviedo (Spain) in 2001. After finishing his Ph.D., he spent some time as a post-doctoral research associate at the Laboratory for Electromagnetic and Electronic Systems of the Massachusetts Institute of Technology. Dr. Domínguez-García received the NSF CAREER Award in 2010, and the Young Engineer Award from the IEEE Power and Energy Society in 2012. He is also a Grainger Associate since 2011. He currently serves as an Associate Editor for the IEEE Transactions on Power Systems and the IEEE Power Engineering Letters.